Received: 8 November 2023 | Revised: 11 June 2024 | Accepted: 11 July 2024

DOI: 10.1002/pro.5124

RESEARCH ARTICLE

THE PROTEIN SOCIETY WILEY

Integrating molecular dynamics simulation with small- and wide-angle X-ray scattering to unravel the flexibility, antigen-blocking, and protease-restoring functions in a hindrance-based pro-antibody

Jun Min Liao[1] | Shih-Ting Hong[2] | Yeng-Tseng Wang[3] | Yi-An Cheng[1,4,5] | Kai-Wen Ho[1] | Shu-Ing Toh[6] | Orion Shih[7] | U-Ser Jeng[7,8] | Ping-Chiang Lyu[9] | I-Chen Hu[9] | Ming-Yii Huang[2,10] | Chin-Yuan Chang[4,6,11] | Tian-Lu Cheng[1,2,4,12]

Correspondence
Chin-Yuan Chang, Graduate Institute of Medicine, College of Medicine, Kaohsiung Medical University, Kaohsiung 80708, Taiwan.
Email: cycytl@nycu.edu.tw

Tian-Lu Cheng, Drug Development and Value Creation Research Center, Kaohsiung Medical University, Kaohsiung 80708, Taiwan.
Email: tlcheng@kmu.edu.tw

Funding information
Ministry of Science and Technology, Grant/Award Numbers: MOST 110-2320-B-037-010-MY3, MOST 111-2124-M-037-001-MY3, MOST 111-2314-B-037-051-MY3; KMU-KMUH Co-Project of Key Research, Grant/Award Numbers: KMUH-DK(B)110004-3, KMUH-DK(B)110006-1, KMUH-DK(B)110006-2, KMUH-DK(B)111004-2, KMUH-DK(B)111001-3, KMUH-DK(B)112001-2; Kaohsiung Medical University, Grant/Award Numbers: KMU-DK(B)110004-2, KMU-DK(B)111004, KMU-DK(B)111001-2, KMU-DK(B)112001-1, KMU-DK(B)112001-3, KMU-TC112A03; NTHU-KMU Joint Research Project, Grant/Award Numbers: KT112P002, KT113P004

Abstract

Spatial hindrance-based pro-antibodies (pro-Abs) are engineered antibodies to reduce monoclonal antibodies' (mAbs) on-target toxicity using universal designed blocking segments that mask mAb antigen-binding sites through spatial hindrance. By linking through protease substrates and linkers, these blocking segments can be removed site-specifically. Although many types of blocking segments have been developed, such as coiled-coil and hinge-based Ab locks, the molecular structure of the pro-Ab, particularly the region showing how the blocking fragment blocks the mAb, has not been elucidated by X-ray crystallography or cryo-EM. To achieve maximal effect, a pro-Ab must have high antigen-blocking and protease-restoring efficiencies, but the unclear structure limits its further optimization. Here, we utilized molecular dynamics (MD) simulations to study the dynamic structures of a hinge-based Ab lock pro-Ab, pro-Nivolumab, and validated the simulated structures with small- and wide-angle X-ray scattering (SWAXS). The MD results were closely consistent with SWAXS data ($\chi^2_{\text{best-fit}} = 1.845$, $\chi^2_{\text{allMD}} = 3.080$). The further analysis shows a pronounced flexibility of the Ab lock (root-mean-square deviation = 10.90 Å), yet it still masks the important antigen-binding residues by 57.3%–88.4%, explaining its 250-folded antigen-blocking efficiency. The introduced protease accessible surface area method affirmed better protease efficiency for light chain (33.03 Å^2) over heavy chain (5.06 Å^2), which aligns with the experiments. Overall, we developed MD-SWAXS validation method

Jun min Liao and Shih-Ting Hong contributed equally to this study.

For affiliations refer to page 15

Review Editor: Lynn Kamerlin

to study the dynamics of flexible blocking segments and introduced methodologies to estimate their antigen-blocking and protease-restoring efficiencies, which would potentially be advancing the clinical applications of any spatial hindrance-based pro-Ab.

KEYWORDS

antibody engineering, antibody lock, molecular dynamics simulation, protein science, small- and wide-angle X-ray scattering

1 | INTRODUCTION

MAbs have shown great promise in treating various diseases due to their exceptional binding affinity and specificity. However, their inability to discriminate between antigens in healthy and diseased tissues can lead to on-target toxicity (Tang et al., 2023). For instance, antibodies like Ipilimumab (anti-CTLA-4 Ab) and Nivolumab (anti-PD-1 Ab) targeting CTLA-4/PD-1 have been associated with severe immune-related adverse events, including hepatitis, colitis, thyroid disorders, and, in rare cases, paralysis (Nixon et al., 2017). Similarly, antibody drugs for rheumatoid arthritis, such as Infliximab and Adalimumab (anti-TNFα Ab) targeting TNFα, can induce grave infections, reactivate latent viruses like hepatitis or herpes zoster, and even increase malignancy risk (Cludts et al., 2017). To address this issue, activatable antibodies (pro-antibodies, pro-Abs) have been developed to localize the action of the antibody exclusively to diseased regions (Lucchi et al., 2021). Such strategies include light activatable antibodies (Self & Thompson, 1996), pH activatable antibodies (Biewenga et al., 2023), and protease-activatable antibodies (Desnoyers et al., 2013; Donaldson et al., 2009; Lu et al., 2019; Trang et al., 2019). Protease-reactive pro-Abs, in particular, has been extensively studied due to the tumor heterogeneity observed in cancer cells, which is characterized by the expression of various proteases (Habič et al., 2021). These protease-reactive pro-Abs remain inactive until activated at protease-rich disease sites, ensuring targeted therapeutic action. Structurally, these pro-Abs incorporate a blocking segment that links mAbs via protease substrates and linker peptides. Previous works, such as those by Desnoyers et al. (2013) and Donaldson et al. (2009), employed affinity-based blockers like binding peptides and antigen fragments to obscure the antigen-binding domain. However, fine-tuning the affinities of these segments for optimal antigen-binding and subsequent protease-mediated removal necessitates complicated redesigns for each mAb variant. Consequently, spatial hindrance-based blocking segments have gained traction as a more versatile solution. Trang et al. (2019) showed an example by using coiled-coil domains combined with matrix metalloproteinase-2/9 (MMP-2/MMP-9) cleavable substrates to mask a CD19-binding Ab hBU128. Lu et al. (2019) introduced an "Ab lock" strategy: leveraging an antibody's native hinge region and linking the N-terminals of mAbs through MMP-2/MMP-9 substrates and peptides to form a pro-Infliximab, concealing Infliximab's antigen-binding site. Pro-Infliximab reduced binding affinity by 395-fold, was reactivated only in disease locales, and demonstrated minimal immunogenicity in both murine and human cellular models (Lu et al., 2019). Notably, this is the only pro-Ab documented with low immunogenicity. However, some spatial hindrance-based pro-Abs still struggle with low antigen-blocking or protease-restoring efficiency. Further optimization of them by modifying linker peptides requires the structural information about the interactions between the Ab lock and the complementarity-determining region (CDR). While elucidating pro-Ab structures is important, X-ray crystallography (Schneidman-Duhovny et al., 2014; Van Den Bedem & Fraser, 2015) and cryo-EM (Punjani & Fleet, 2021; Villarreal & Stewart, 2014) face challenges with flexible blocking segments. Thus, an alternative methodology to decode their structures is necessary.

To solve the structure of pro-Abs, we employed a molecular dynamics (MD) simulation to investigate their dynamic motions and compared the resulted trajectories with small- and wide-angle X-ray scattering (SWAXS) data. MD simulation provides possible molecular structural information, and SWAXS provides further experimental evidences. Their combination is an effective confirmation at revealing the conformational features of highly flexible proteins (Lin et al., 2021; Röllen et al., 2018; Schumann et al., 2022; Song et al., 2018; Yang et al., 2009; Zhou et al., 2018). In this study, we selected a hinge-based Ab lock pro-Ab of Nivolumab (pro-Nivolumab), which represents good antigen-blocking and protease-restoring efficiencies (Huang et al., 2021), as a representative example for our investigation. The study began with an evaluation of the antigen-blocking capability and protease-restoring efficiency of the substrate regions on the light chain (LC) and heavy chain (HC) of

the pro-Nivolumab Immunoglobulin G (IgG) using enzyme-linked immunosorbent assay (ELISA) and Western blot, respectively. Subsequently, we employed the MD simulations to derive its dynamic structures and parallelly preformed SWAXS experiment to validate the MD simulations of the pro-Nivolumab fragment antigen-binding (Fab). In the validation, the simulated SWAXS profiles of MD trajectories were generated using ATSAS CRYSOL software (Manalastas-Cantos et al., 2021; Svergun et al., 1995) and then compared to the experimental SWAXS data. Our investigation had three specific objectives: (1) to examine the flexibility of the Ab lock, evaluate the root-mean-square deviation (RMSD), and visualize its movements and distribution through structural cluster analysis; (2) to validate the antigen-blocking capability via calculating cover rates of the antigen-binding residues and reveal the Ab lock's structural features through structural cluster analysis; and (3) to develop a surface-area-based methodology, termed as protease accessible surface area (PASA), to estimate the protease cleavage efficiency of LC and HC and validate the methodology with docking simulations. By successfully determining the mobile structures of pro-Abs and developing the methodologies to estimate the antigen-blocking capability and protease-restoring efficiencies, it will be possible to optimize the designs of pro-Abs in the future, addressing the issues of low antigen-blocking and protease-restoring abilities. This breakthrough may potentially accelerate the development and commercialization of pro-Abs.

2 | RESULTS

2.1 | Evaluation of antigen-binding ability and protease cleavage efficiency of pro-Nivolumab IgG

To evaluate the antigen-binding ability of pro-Nivolumab IgG, the pro-Nivolumab IgG and Nivolumab IgG were subjected to incubation with or without MMP-2 for 1 h and then added to a PD-1-coated ELISA plate. Subsequently, the setup was stained with goat anti-human IgG Fc-HRP and ABTS was added to evaluate the antigen-binding ability through absorbance at 405 nm. The result revealed significant differences in the half maximal effective concentration (EC_{50}) for pro-Nivolumab IgG (75 nM) and pro-Nivolumab IgG with MMP-2 (0.3 nM) (Figure 1a), suggesting 250-fold reduced antigen-binding ability in pro-Nivolumab IgG. Moreover, MMP-2 treatment restored the antigen-binding ability of pro-Nivolumab IgG to the level of Nivolumab IgG (Figure 1a, blue line). To evaluate the protease cleavage efficiencies of the LC and HC of pro-Nivolumab IgG, we examined molecular weight changes by Western blot. Pro-Nivolumab IgG and MMP-2 were incubated in a 250:1 molar ratio over varying time periods. The theoretical molecular weights of pro-Nivolumab IgG's LC before and after the protease cleavage are 26,447.40 and 24,067.78 Da, while those of pro-Nivolumab IgG's HC are 51,990.49 and 48,941.14 Da. Figure 1b shows a time-dependent substrate cleavage by MMP-2. A quantitative analysis of the cleaved and uncleaved bands of the LC and HC, performed using the Gel-Pro Analyzer software, revealed that 96% and 27% substrates in the LC and HC were cleaved following incubation for 60 min with MMP-2 (Figure 1c), indicating that the protease cleavage efficiency of the LC is higher than HC in pro-Nivolumab IgG. The raw data of this ELISA and Western blot experiments are attached in Figures S1 and S2. Mass spectrometry (MS) was also employed to verify these molecular weight alterations (Figure S3). Using 4 mM DTT to break the disulfide bonds connecting HC and LC, the result of matrix-assisted laser desorption/ionization-MS (MALDI-MS) showed two peaks at 52,878.271 and 26,448.361 m/z before the MMP-2 cleavage, corresponding to the HC and LC in the pro-Nivolumab IgG, respectively. After proteolysis, the two peaks decreased to 48,267.445 and 24,100.511 m/z, indicating that the Ab lock had been cleaved.

2.2 | Structural determination of pro-Nivolumab Fab by MD simulations and SWAXS

Our preliminary studies on the structure of Pro-Nivolumab Fab were using X-ray crystallography and cryo-EM. According to the X-ray diffraction spectra, only few parts of the Ab lock structure can be resolved because the electron density is too sparse. The study by cryo-EM showed not enough images to build the structure of Ab lock. Both results indicated the high flexibility of the Ab lock in pro-Nivolumab. To understand the highly flexible structure of the pro-Nivolumab Ab lock, we utilized MD simulations to model the structures of pro-Nivolumab Fab. Then, the corresponding scattering patterns of all snapshots of MD simulations are derived and compared with SWAXS data of the pro-Nivolumab Fab. In MD simulations, we constructed a model of the pro-Nivolumab Fab by attaching the Ab lock on the resolved crystal structure of Nivolumab (PDB (Burley et al., 2022) ID: 5GGQ (Lee et al., 2016)), and then performed 64 sets of repeated 200 ns MD simulations, using AMBER22 pmemd.cuda program (Case, Duke, et al., 2022) under 300 K NVT ensembles with TIP3P

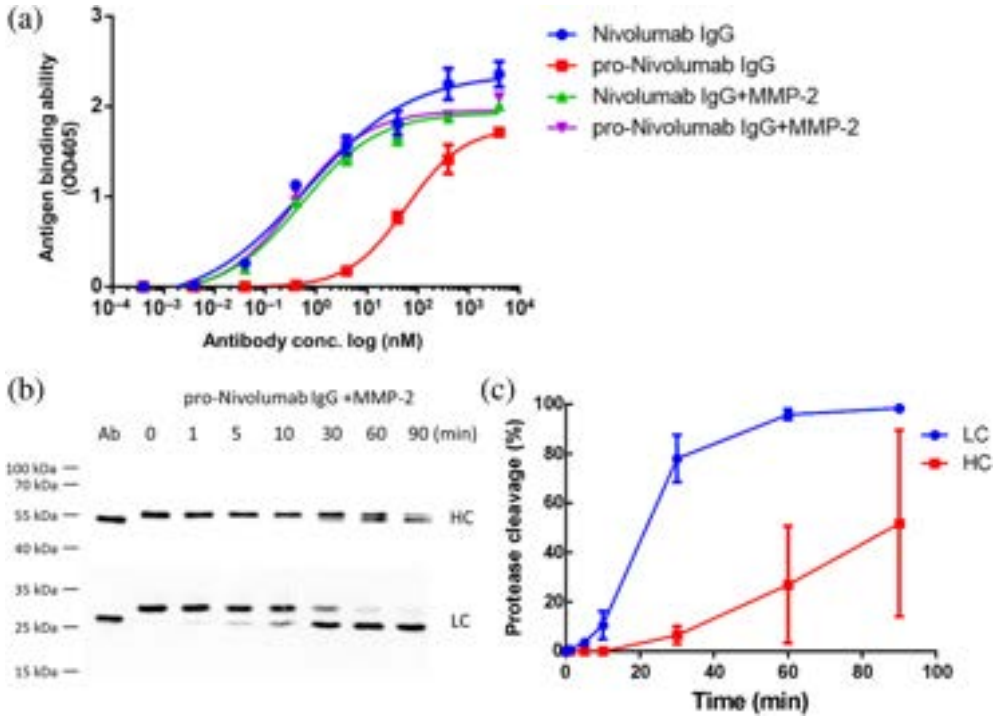

FIGURE 1 Antigen-blocking capability and protease cleavage efficiency of pro-Nivolumab Immunoglobulin G (IgG) (a) The antigen-binding ability of Nivolumab IgG (blue line), Nivolumab IgG + matrix metalloproteinase-2 (MMP-2) (green line), pro-Nivolumab IgG (red line), and pro-Nivolumab IgG + MMP-2 (purple line) was assessed by PD-1-based enzyme-linked immunosorbent assay. (b) A detailed investigation of cleavage progression over time: 1.11 μg of pro-Nivolumab IgG was incubated with 2 ng of recombinant human MMP-2 in a 250:1 ratio at 37°C for 0, 1, 5, 10, 30, 60, and 90 min. The levels of pro-Nivolumab IgG's LC and HC that were cleaved and uncleaved were discerned using goat anti-human IgG F(ab')$_2$-HRP and goat anti-human IgG Fc-HRP, respectively, with Western blot. (c) Band quantification from panel (b) and Figure S2B: Percentages of cleaved and uncleaved pro-Nivolumab light chain (LC) and heavy chain (HC) were quantified using Gel-Pro software. The data represent two independent experiments. Error bars indicate standard deviation.

waters, to simulate the dynamic trajectories of pro-Nivolumab. The theoretical SWAXS profile of each MD snapshot was generated by using ATSAS CRYSOL 3.2 (Svergun et al., 1995). In SWAXS experiments, the purified pro-Nivolumab Fab at a concentration of 10 mg/mL in 20 mM Tris and 100 mM NaCl (pH 8) was submitted for SWAXS analysis at the TPS 13A beamline of the National Synchrotron Radiation Research Center (Taiwan) (Liu et al., 2021; Shih et al., 2022). The wide-angle X-ray scattering (WAXS) data were applied to probe smaller structural features of the Ab lock. Subsequently, the results revealed a high degree of congruence between the MD and SWAXS. Figure 2a shows that the best-fit MD model (red line) aligns with the experimental SWAXS data (blue dots), presenting a chi-square (χ^2) value of 1.334. The averaged MD SWAXS profiles (black line), produced by averaging all generated theoretical SWAXS profiles, also corresponded with a χ^2 value of 2.457. Notably, the calculated radius of gyration from the SWAXS data was 29.14 Å, nearly identical to the radius of gyration derived from both the best and averaged MD models, which stood at 29.15 Å. To provide further fitting against the MD trajectories, we performed the ensemble optimization method (EOM) to fit the SWAXS data with MD trajectories. Using our homemade genetic algorithm program, we found ensembles of the MD trajectories fits better than single best MD model, presenting a χ^2 value of 1.304 (Figure 2a, green line), further supporting that Ab lock is flexible and existing as structural mixtures in the solution. Figure 2b shows the volume fractions of the ensembles, and Figure 2c,d show their structures. If comparison is taken only within the SAXS range (max $q = 0.5$ Å^{-1}), the EOM further decreases the χ^2 value from 1.225 to 1.204 (Figure S4). These observations strongly suggest that the MD-simulated structures are highly supported by the SWAXS results, indicating that we successfully simulated the flexible structures of the Ab lock in pro-Nivolumab.

2.3 | Exploring the mobile features of the pro-Nivolumab Ab lock using SWAXS and MD simulations

To analyze the mobility exhibited by the Ab lock within pro-Nivolumab, we used two analytical

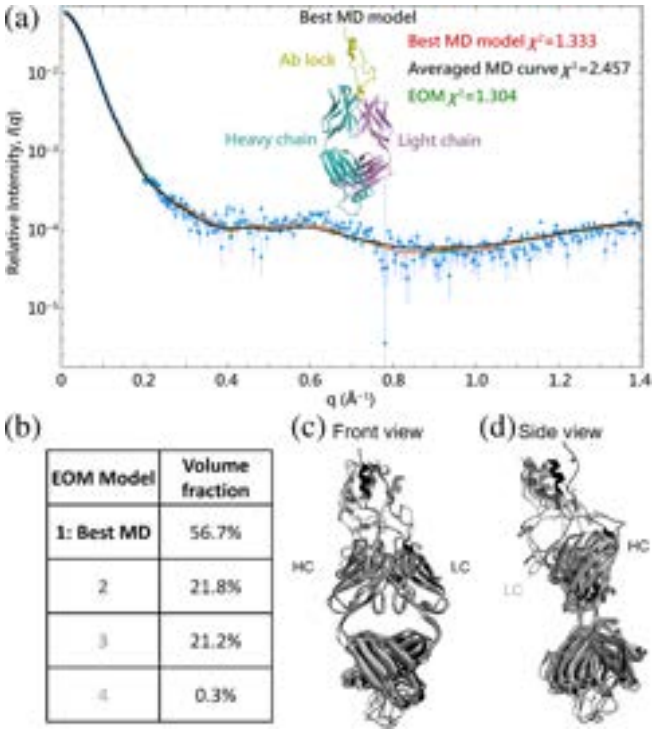

EOM Model	Volume fraction
1: Best MD	56.7%
2	21.8%
3	21.2%
4	0.3%

FIGURE 2 The best-fit molecular dynamics (MD) model, ensemble optimization method (EOM) and all MD trajectories aligns with small- and wide-angle X-ray scattering (SWAXS) data. (a) The SWAXS data of a wide-q range are fitted with the scattering profile of the best-fit MD model (red line, $\chi^2 = 1.334$), the solved ensemble from EOM (green line, $\chi^2 = 1.304$) and the average of all MD trajectories' scattering profiles (black line, $\chi^2 = 2.457$). This close fit indicates that the reliability of our MD simulations is highly supported by the SWAXS experimental data. The model displayed in the figure is the best-fit MD model in which the Ab lock region is shown in yellow, and the HC and LC are shown in cyan and purple, respectively. (b) The volume fractions of the solved ensemble. (c) and (d) offer front and side views of the EOM models, respectively. Models with higher volume fractions are represented in darker, indicating that the Ab lock components within the ensemble predominantly occupy the central region.

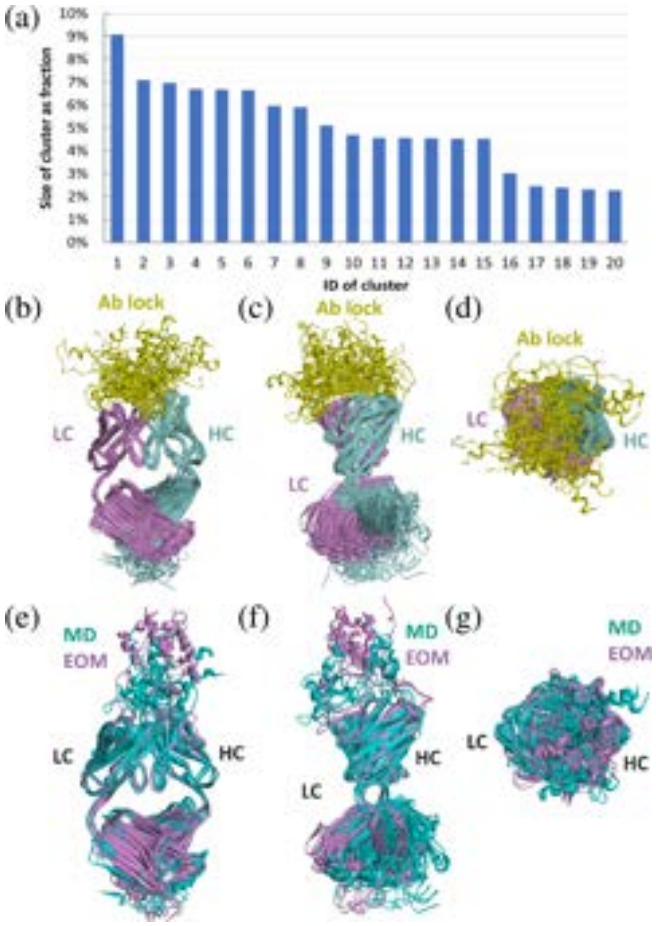

FIGURE 3 Superposition of 20 clusters categorized by root-mean-square deviation of the Ab lock's structures. (a) The distribution percentages of 20 clusters by K-means algorithm. (b) The front view, (c) the side view and (d) the top view of the 20 superimposed cluster structures. The structures of the Ab lock are positioned above the complementarity-determining region and extend in various conformations without a stable tertiary structure. (e) The front view, (f) the side view, and (g) the top view of the comparison between best 5 molecular dynamics (MD) clusters' models and ensemble optimization method (EOM) models. Both MD and EOM models show similar spatial distributions of the Ab lock, consistently showing placement primarily in the middle, which aligns with experimental data. HC, heavy chain; LC, light chain.

approaches. First, we applied a RMSD analysis to assess the mobile conformation of the Ab lock. The averaged calculated overlapping RMSD of the Ab lock among the MD trajectories was found to be 10.90 Å. Considering that one end of the Ab lock is anchored to the N-terminal of the LC and HC, this RMSD indicates notable mobility in its structure (Martínez, 2015). To represent MD trajectories and visualize the variety in conformations, we categorized all MD trajectories into 20 distinct structural clusters based on the RMSD of the Ab lock's Cα atoms using K-means algorithm (Likas et al., 2003). As shown in Figure 2a, these clusters are distributed from 9.07% in cluster #1 to 2.27% models in cluster #20. The graphical representations in Figure 3b–d provide front, side, and top views, respectively, of 20 representative models of the clusters superimposed based on the variable region of the Fab. The figures show the Ab lock positioning above the CDRs, extending in diverse directions, and not adopting any stable tertiary structure. Collectively, these results show the Ab lock possesses very high levels of flexibility. Figure 3e–g presents a comparative analysis of the first five clusters' representative MD models with EOM models. While both approaches demonstrate that the Ab lock is positioned over the middle of the CDRs

with the similar spatial distributions. This confirms that the MD models are effective in reflecting the ensemble behaviors captured through EOM.

2.4 | Structural analysis and antigen-blocking capability of the pro-Nivolumab Ab lock

To clarify why the mobile Ab lock of pro-Nivolumab still inhibits antigen binding affinity by 250-fold, it is necessary to trace the trajectory of the Ab lock to understand how it positions above the CDRs. Therefore, we used our molecular structure computational simulation estimation methodology (Huang et al., 2021) to calculate the cover rate of each CDR residue. A residue was counted as "covered" by the Ab lock if any atom of the Ab lock was above 120° of it and within 4 Å, which is an appropriate distance for long-range atomic interactions. The cover rates were derived from the frequencies of cover through all MD trajectories. Figure 4a displays a red color-coded heatmap of cover rates and the black labels show the antigen-binding residues of pro-Nivolumab. Higher cover rates are indicated by deeper red color. Notably, the region at the middle of the LC and HC, where most antigen-binding residues are located, is extensively covered by the mobile Ab lock. Figure 4b details the corresponding cover rates for each binding residue. It reveals that common binding amino acids, such as Tyrosine (Y) and Tryptophan (W), are highly covered by the Ab lock. The binding residues on the HC CDR1 and CDR2, including H30S, H31N, H33G, H52W, and H53Y, exhibit high cover rates (57.3%, 80.9%, 62.9%, 57.9%, and 70.7%, respectively). Similarly, in HC CDR3, H99N, H100D, and H102Y are extensively covered (71.5%, 88.4% and 86.7%, respectively). On the LC, L32Y has a high cover rate of 77.6%. Overall, the antigen-binding residues around the central groove between LC and HC are covered by 57.3%–88.4%. These patterns suggest that the Ab lock traverses through the central groove between the LC and HC and covers several crucial antigen-binding residues with its mobile structure. This is visualized in Figure 4c,d, which shows the side and the top view of the 20 superimposed cluster structures of the Ab lock on a color-coded surface of Nivolumab. The figure demonstrates how the Ab lock chains of the LC and HC traverse the central groove of CDR, converge by the disulfide bonds, and progress upwards. Therefore, the mobile Ab lock can still efficiently block the antigen-binding affinity of pro-Nivolumab by 250-fold without the necessity for a stable conformation. The corresponding superimposed molecular structure is provided in PDB format in File S1.

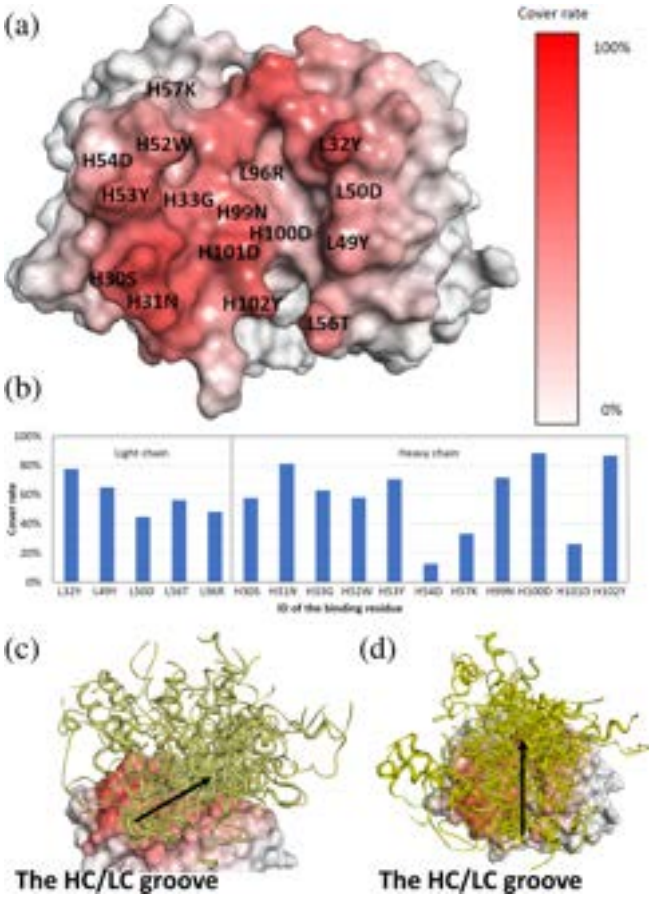

FIGURE 4 Cover rates and antigen-binding residues of pro-Nivolumab, and the superimposed cluster structures of the Ab lock. (a) A heatmap of cover rates (represented in red) and the antigen-binding residues (represented with black labels) of pro-Nivolumab; the antigen-binding residues around the central groove are covered to a large extent by the Ab lock. (b) A bar chart displaying the cover rates of the antigen-binding residues of pro-Nivolumab. (c) The side view and (d) the top view of the superimposed images of 20 cluster structures on the heatmap of cover rates, showing how the Ab lock traverses the groove between the light chain (LC) and heavy chain (HC), where most antigen-binding residues are located.

2.5 | Development of PASA method to evaluate different protease cleavage efficiencies of the substrates in the pro-Nivolumab LC and HC

To understand the differential cleavage efficiencies of MMP-2 on the pro-Nivolumab LC and HC protease substrates, we employed a twofold strategy; first, we developed an estimation method, we termed PASA, for rapid estimation and then validated the concept of PASA using docking simulations. First, to develop PASA to estimate the protease cleavage efficiency of all MD trajectories, the accessibilities of protease substrates were measured by using a spherical probe in a radius to the reaction core of

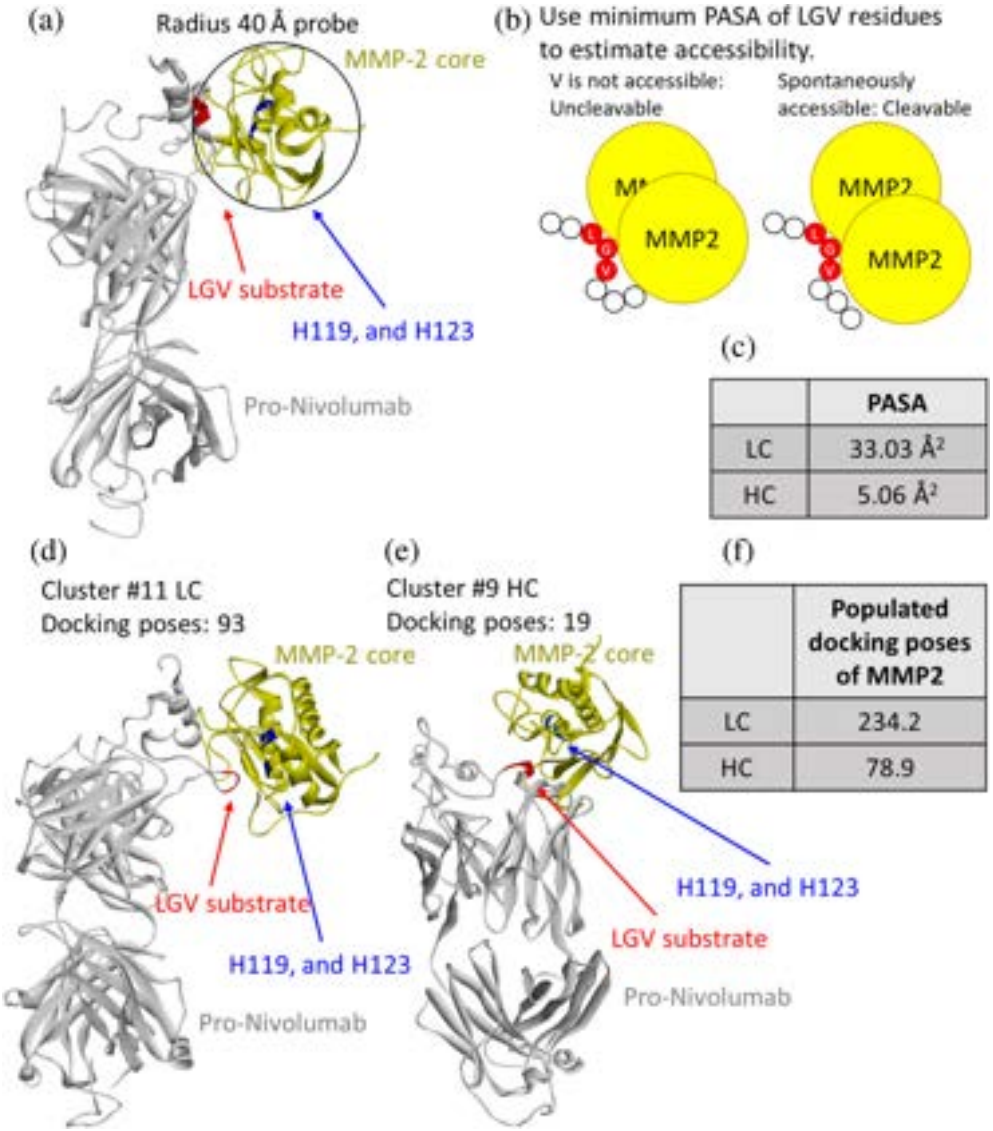

FIGURE 5 Illustration of the protease accessible surface area (PASA) calculation method, the computed PASA of the light chain (LC) and heavy chain (HC) in pro-Nivolumab, and the docking outcomes of matrix metalloproteinase-2 (MMP-2) onto LC and HC substrates on 20 representative cluster structures. (a) The size of the probe is set to match the radius of the MMP-2 protease (40 Å), where the pro-Nivolumab is shown in white, MMP-2 is shown in yellow, the black-lined circle demonstrates the radius of probe, the LGV residues of LC or HC are shown in red, and MMP-2 catalytic sites (H119 and H123) are shown in blue. (b) The PASA for the LC and HC substrates is determined by considering the minimum value of the LGV residues (red circles), indicating their potential to contact with the protease simultaneously. (c) The pro-Nivolumab LC substrate has a PASA of 33.03 $Å^2$, while the HC substrate has a PASA of 5.06 $Å^2$. (d) The best cluster of LC #11 shows 93 MMP-2 docking poses. (e) The best cluster of HC #5 shows 19 MMP-2 docking poses. (f) The population-adjusted docking poses of MMP-2 on 20 cluster representative structures show that 234.2 MMP-2 poses bind to the LC substrate and 78.9 MMP-2 poses bind to the HC substrate. Both the PASA and docking results are consistent with experimental findings in which the LC in pro-Nivolumab is more prone to cleavage than the HC.

MMP-2 (40 Å, derived from PDB:3AYU), as illustrated in Figure 5a. To ensure the protease can spontaneously access all necessary residues of the substrates, we analyzed the minimum PASA of the LGV residues, which are most crucial for MMP-2 cleavage, to exclude uncleavable conformations (Figure 5b). Therefore, a higher PASA indicates increased accessibility of the substrate to MMP-2, thereby enhancing the cleavage efficiency. Figure 5c shows the results, indicating that the LC substrate has a larger PASA (33.03 $Å^2$) than the HC substrate (5.06 $Å^2$), indicating the LC is more susceptible to cleavage than the HC. This result aligns with the experimental protease cleavage efficiencies presented in Figure 1c. Subsequently, to validate the effectiveness of the PASA

(a)

Pro-Abs	EC50 (−/+MMP-2) (nM)	Antigen-blocking folds	Cover rates of binding residues	Estimated half-lives within MMP-2 (LC/HC) (min)	Cleavage reaction rate (LC/HC) (M/min)	PASA (LC/HC) (Å²)
Pro-Nivolumab	75/0.3	250	73.43%	8/30	0.0158/0.0042	33.1/5.06
Pro-Nivolumab-2	60/0.8	75	67.50%	8/170	0.0158/0.0007	18.16/0.25
Pro-Urelumab-1	4/0.2	20	67.74%	12/30	0.0105/0.0042	467.7/135.2
Pro-Urelumab-2	9/0.2	45	70.28%	15/220	0.0084/0.0006	464.4/60.0

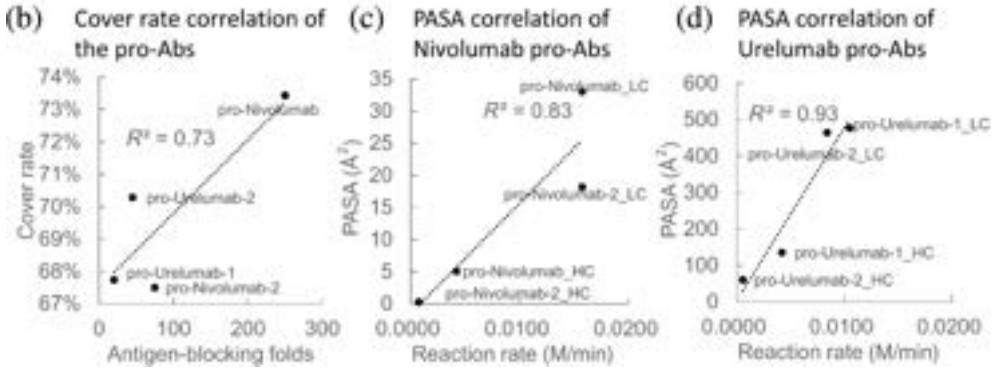

FIGURE 6 Evaluation of antigen-blocking and protease-restoring efficacies in pro-antibodies (pro-Abs). (a) the half maximal effective concentration (EC_{50}), antigen-blocking folds, cover rates, estimated half-lives, cleavage reaction rates, and protease accessible surface area (PASA) estimations of the extended experiments. (b) Cover rates are correlated ($R^2 = 0.73$) with antigen-blocking folds. (c) PASAs are correlated ($R^2 = 0.83$) with the cleavage reaction rates for Nivolumab pro-Abs. (d) A correlation ($R^2 = 0.93$) is found between PASA and cleavage reaction rates for Urelumab pro-Abs. Together, these results affirm the effectiveness of our computational approaches in accurately predicting the antigen-blocking capabilities and protease cleavage efficiencies of pro-Abs. HC, heavy chain; MMP-2, matrix metalloproteinase; LC, light chain.

methodology, we deployed actual MMP-2 molecules instead of a spherical probe to evaluate substrate accessibility. This was achieved through a docking analysis conducted using the HDOCK (Yan et al., 2020) and the MMP-2 crystal structure (PDB: 7XJO:A (Takeuchi et al., 2022)) on 20 cluster structures of pro-Nivolumab. Performing docking simulations on all MD trajectories would be excessively time-consuming, so we selected representative models derived from MD clustering to represent the MD trajectories. Our docking simulation criteria were set with a distance threshold within 6 Å, allowing for an approximation of flexible accessibility rather than precise atomic-level docking. To ensure the substrate is accessible by MMP-2, the LGV residues of substrates must be within 6 Å of the MMP-2 catalytic site (H119 and H123). Each MMP-2 pose is expected to be displaced at least 5 Å RMSD, thereby allowing us to estimate the accessibilities of substrates based on the number of resulting docking poses. For visual comprehension, examples of most resulting docking poses of LC and HC are presented. Figure 5d demonstrates the most cleavable cluster of the LC, with the LC substrate being highly exposed, accessible by 93 MMP-2 poses. Figure 5e shows the most cleavable cluster of the HC, accessible by 19 docking poses of MMP-2. The numbers of docking poses were then multiplied by the relative population of the representative MD clusters and summarized. Figure 5f summarizes the docking results of the 20 clusters, indicating more binding possibilities for the LC substrate (234.2 poses) than for the HC substrate (78.9 poses), suggesting that the LC substrate is more accessible and prone to cleavage. The results from docking agree with the PASA methodology, indicating the PASA methodology can be used to evaluate the accessibility of protease substrates to facilitate the reactivating ability of pro-Abs.

2.6 | Assessing the precision of antigen-blocking and protease cleavage efficiency estimation methods

To assess the predictive accuracy of our computational cover rate and PASA estimation methods, an additional set of pro-Abs—original pro-Nivolumab, pro-Nivolumab-2, pro-Urelumab-1, and pro-Urelumab-2—were included in the experiments. These pro-Abs were analyzed by ELISA, Western blot, MD simulations, cover rate, and PASA estimations with the method that described as in pro-Nivolumab. Presented in Figure 6a are the EC50 values, antigen-blocking folds, cover rates of binding residues, estimated half-lives ($t_{1/2}$, reaction time of 50/50 cleavage) under MMP-2 treatment, calculated protease cleavage reaction rates, and PASAs for the

pro-Abs in which the protease cleavage reaction rates were calculated by secondary reaction equation and half-lives (see Section 4). A notable correlation between antigen-blocking folds and cover rates for the pro-Abs is demonstrated in Figure 6b ($R^2 = 0.73$). This outcome affirms our cover rate estimations in evaluating antigen-blocking capacities of pro-Abs, which was also previously verified in earlier publication (Huang et al., 2021). To evaluate the predictive accuracy of PASA estimations, we derived the cleavage reaction rates from the estimated half-lives of the pro-Abs' LC and HC. The correlation of PASA estimations and cleavage reaction rates for the Nivolumab and Urelumab pro-Abs are shown in Figure 6c,d, respectively. These figures highlight a meaningful correlation $R^2 = 0.83$ and 0.93 for Nivolumab and Urelumab pro-Abs, respectively, indicating that the PASA estimations and cleavage reaction rates are correlated across different pro-Abs. By these correlations, we demonstrated the robustness of our computational strategies in accurately predicting the antigen-blocking capabilities and protease cleavage efficiencies of pro-Abs, which is useful in guiding the development of pro-Abs.

3 | DISCUSSION

In this study, we used MD simulation to elucidate the intricate mobile structures of the flexible Ab lock in pro-Nivolumab and validated the simulation with SWAXS experiment. This MD-SWAXS combining method is able to overcome the limitations of X-ray crystallography and Cryo-EM in investigating flexible protein regions. We discovered that the Ab lock had a unique mobile feature as a blocking segment with an RMSD of 10.90 Å even when its C ends are anchored on the mAb. Moreover, by calculating the cover rates of individual antigen-binding residues, we found that the mobile Ab lock invariably traverses the central groove of the CDR, resulting in the blocking of several crucial antigen-binding residues. This blocking mechanism is responsible for the substantial reduction (250-fold) in antigen-binding affinity. We also devised a novel evaluation methodology, termed PASA, to examine the protease cleavage efficiency of each substrate. This PASA methodology was further validated by docking simulations. The results revealed that the LC is more cleavable than the HC, which is consistent with experimental outcomes. In a later chapter, we examined additional pro-Abs, affirming the precision of our computational strategies in accurately predicting the antigen-blocking capabilities and protease-restoring efficiencies of pro-Abs. These two evaluation methodologies, coupled with the MD-SWAXS method for structural determination, enabled us to comprehensively investigate the structures and functionalities of pro-Abs and also paves the way for the establishment of a robust computational system. This allows us to optimize the antigen-blocking capability and protease-restoring efficiency of pro-Abs by modifying the composition of linker peptides, and could potentially allow us to overcome the efficiency problem and transform any mAb into a pro-Ab, thereby reducing the on-target toxicity. As such, our achievements represent a significant milestone for the hindrance-based pro-Abs, potentially accelerating their commercial development.

Understanding the structure of highly flexible proteins, also known as intrinsically disordered proteins, is vital in the field of biological chemistry. Flexible proteins are widespread in eukaryotic organisms (Wright & Dyson, 2015); they play critical roles in protein function, regulation, and interaction networks (Uversky, 2013). However, it is challenging to resolve the structures of flexible proteins via the traditional methods such as X-ray crystallography (Schneidman-Duhovny et al., 2014; Van Den Bedem & Fraser, 2015) or cryo-EM (Punjani & Fleet, 2021; Villarreal & Stewart, 2014) because they do not stay uniform to diffract enough electron density or provide repeated images. For example, flexible hinge regions are hard to resolve unless they are immobilized (Harris et al., 1997, 1998; Scapin et al., 2015). On the other hand, NMR techniques have upper size limits around 50 kDa; thus, larger structures present a challenge (Klein et al., 2022). Furthermore, the high flexibility of the Ab lock causes severe spectral overlaps in NMR spectrum, further increasing the complexity of structural determinization (Piai et al., 2014). Due to these limitations, we explored the structure of the Ab lock in pro-Nivolumab by employing an integrated MD-SWAXS method. This MD-SWAXS method can be applied to other proteins containing flexible regions, including other pro-Ab techniques, providing a useful tool to enrich our understanding of their structural and functional roles.

In biological systems, extensive flexibility is often associated with immune evasion. This mechanism has been found in several viruses. For example, in the HIV-1 gp120 protein, the structural flexibility of its V1/V2 regions may prevent recognition by the CD4 immune response cells (Lavie et al., 2018). Similarly, the hepatitis C virus is believed to exploit the structural flexibility of its E2 epitope for immune evasion (Drummer, 2014). The S2 protein in SARS-CoV-2 has also been suggested to employ such a mechanism (Gupta, 2022; Meng et al., 2021; Tian et al., 2022). This link between high flexibility and low immunogenicity has been explored in the work of Peter et al., who performed a series of simulations demonstrating this inverse relationship (Joshi et al., 2011). They also developed a protein flexibility-based algorithm for B-cell

epitopes (Tian et al., 2022). This correlation might be applicable to our pro-Abs because the Ab lock displays extremely high flexibility. Indeed, our pro-Infliximab would not instigate an immune response in mice (Lu et al., 2019), reinforcing the potential of low immunogenicity of pro-Abs. Several web tools, including IEDB (Mendes et al., 2023) and BCEPS (Ras-Carmona et al., 2021), offer preliminary insight into predicting potential B-cell epitopes. Interestingly, our Ab lock does not appear to present any corresponding B-cell epitopes in these predictive models. Given these findings, we hypothesize that the high flexibility of the Ab lock could contribute to low immunogenicity of pro-Abs. This flexibility, coupled with the endogeneity of the hinge regions, could make our Ab lock an ideal strategy for long-term mAb treatments, reducing the likelihood of an immune response, potentially making the Ab lock an outstanding modification for pro-Abs.

The antigen-blocking capability of a pro-Ab plays a critical role in minimizing the on-target toxicity of mAbs. To enhance this capability, we previously devised a computational system to calculate the averaged cover rates of CDRs, revealing a positive correlation between cover rates and reduction ratios of binding affinities (Huang et al., 2021). In the original method, we purposely avoided incorporating the information of antigen-binding residues, which allowed us to compare the capability of binding affinity reduction across different mAbs even if antigen-binding residues were unknown. In this study, we explored the unique mobile feature of the Ab lock in pro-Nivolumab. This led us to alter our computational system to generate a heatmap of cover rates to track the pathway traversed by the mobile Ab lock. We observed that the Ab lock traverses through the central groove of the CDR and blocks several vital antigen-binding residues. The residues of HC CDR3, frequently considered the most pivotal for antigen binding, were also extensively blocked by the mobile Ab lock. Using this method, we can further optimize the antigen-blocking capability by strategically blocking crucial antigen-binding residues rather than all the CDR. This methodology's efficacy is further supported by additional experiments with Nivolumab and Urelumab pro-Abs, showing an R^2 value of 0.73 for additional pro-Abs tests, indicating that the cover rates of binding residues are in alignment with experimental antigen-blocking measures. This finding validates the precision of our advanced strategy in focusing on binding residues for antigen blocking. These successes will lead to more robust blocking and enable us to minimize the on-target toxicity in mAbs efficiently.

The effectiveness of pro-Abs relies significantly on the protease-restoring efficiency of substrates. Without successful reactivation in the disease region, a pro-Ab cannot deliver its therapeutic benefit. However, protease dysregulation varies across different types of diseases (Eatemadi et al., 2017; Li et al., 2021). For example, MMP-2 is often overexpressed in breast (Li et al., 2017), colon (Dong et al., 2011), and lung cancers (Cao et al., 2017). Urokinase-type Plasminogen Activator (uPA) is often overexpressed in head and neck (Pavón et al., 2016), melanoma (Ilkovitch & Lopez, 2009), gastric (Ding et al., 2013), and prostate cancer (Li & Cozzi, 2007). Hence, to meet disease-specific needs, protease substrates within pro-Abs must be adjustable. Therefore, the development of a computational platform that can evaluate the protease-restoring efficiency based on the structural characteristics of pro-Abs is significant. Until now, the relationship between substrate structure and protease efficiency has remained largely unexplored. Addressing this gap, we introduced the PASA methodology. Its underlying principle is that substrate regions are often blocked by CDR loops or other parts of the Ab lock, impeding access to proteases. Thus, substrate accessibility directly influences the protease reaction rate. Based on this, we integrated the FreeSASA program (Mitternacht, 2016) into our computational system to calculate the accessible surface area of the substrates and tested various probe radii. We identified that a probe with the radius equivalent to the protease's reaction core provided the most accurate estimates. Using PASA, we elucidated the differences in cleavage efficiency between the LC and HC of pro-Nivolumab. The findings, indicating that the LC is more susceptible to cleavage than the HC, aligned well with experimental data, suggesting that we can estimate protease-restoring efficiencies from structural information. To verify the PASA methodology, we performed docking simulations on 20 representative cluster structures, given that due to its time-consuming nature, it would be difficult to apply on all MD trajectories. The docking simulation results aligned well with the PASA, thus validating its efficacy. In the additional tests of Nivolumab and Urelumab pro-Abs, we confirmed the correlation between PASA estimations and protease cleavage rates, showing that the PASA method offers a novel tool for optimizing protease activation of pro-Abs. However, changes in PASA following the cleavage of either the LC or HC were not extensively examined in this study. Despite these postcleavage effects seeming minor in our current analysis, their influence should be investigated in the future. With the PASA methodology, we are now capable of establishing a computational platform for estimating and optimizing protease-restoring efficiency. Coupled with our antigen-blocking estimation methodology, we can construct a computational system that simultaneously optimizes these two crucial pro-Ab functionalities, that is, antigen-blocking capability, and

protease-restoring efficiency by manipulating linker peptides. This system could thus potentially resolve low-performance issues and guide the pro-Ab platform to convert all mAbs into pro-Abs with low on-target toxicity, significantly accelerating future development.

In conclusion, we demonstrated the use of an MD-SWAXS method to reliably investigate the mobile structures of the flexible Ab lock in pro-Nivolumab. The structural analysis showed that the Ab lock is very flexible, with a very high RMSD of 10.90 Å. This high flexibility could possibly account for its low immunogenicity, which would possibly make the Ab lock a promising modification for long-term therapeutic use. Moreover, due to the high flexibility of the Ab lock, we estimated the cover rates of individual CDR residues to trace the Ab lock, and the results showed that the Ab lock traversed the central groove between the LC and HC, blocking several important binding residues with its mobile structure. A new methodology, we named PASA, was innovated to evaluate the protease-restoring efficiencies of the LC and HC substrates. The PASA methodology was validated by docking simulation and the results showed that the LC is more cleavable than HC, aligning with the experimental evidence. Based on this, we assessed the precision of our antigen-blocking and protease cleavage efficiency estimation methods with three new pro-Abs. The results showed robust correlations between computational predictions and experimental outcomes. The consistency observed across different pro-Abs further approve the efficacy of our methodologies in predicting antigen-blocking capabilities and protease cleavage efficiencies. These two methodologies provide insights into the antigen-blocking capability and protease-restoring efficiency of pro-Abs, addressing the performance limitations for certain pro-Abs. The successful resolution of the structure of pro-Nivolumab and the development of functionality evaluations pave the way for the translation of any mAbs to high-quality pro-Abs, which can substantially accelerate the development and commercialization of pro-Abs. Furthermore, the methodology employed here also offers an alternative, promising approach for studying other flexible proteins, highlighting its broad potential applicability in structural biology.

4 | MATERIALS AND METHODS

4.1 | Construction and purification of pro-Nivolumab Fab

The generation of the complementary DNA coding for the LC and HC of pro-Nivolumab Fab was achieved by the utilization of gene synthesis and cloning techniques. In order to enhance the purity of the protein, the C-terminal of the HC was added with TEV protease substrate and His-tag. The 293T cell line was transfected using expression plasmids. Pro-Nivolumab Fab was subjected to protein purification using cOmplete His-Tag Purification Resin (Roche). The His-tagged pro-Nivolumab Fab was subjected to further digestion using TEV protease (Sigma) for overnight at 2–8°C. Subsequently, the Complete His-Tag Purification Resin was employed for the purpose of removing free His-Tag and TEV protease. The pro-Nivolumab Fab that had undergone digestion was introduced into the His-tag purification column, and the resulting flow-through was then collected. To remove high-molecular-weight impurities, the pro-Nivolumab Fab was subsequently introduced into a Gel filtration purification column (HiLoad 16/600 Superdex 75 pg, Cytiva). A 55-KDa fragment of the Pro-Nivolumab Fab was obtained.

4.2 | ELISA for antigen binding ability of pro-Nivolumab IgG

We coated 0.3 μg/mL of human PD-1 protein (Thermo Fisher, A42533) onto an ELISA plate and blocked it with DMEM/2% BSA. 9.6 μL of recombinant human pro-MMP-2 (Sino Biological, 10,082-HNAH, 250 μg/mL) was incubated with 2.4 μL of 10 mM APMA and 12 μL of TCNB buffer (50 mM Tris, 5 mM $CaCl_2$, 150 mM NaCl, 0.05% Brij 35, pH 7.5) at 37°C for 1 h to activate pro-MMP-2 protease. Four thousand nanometer of pro-Nivolumab IgG and Nivolumab IgG were incubated with or without activated MMP-2 at 37°C for 1 h, and BCS was added to stop the reaction. All samples ($n = 2$) with serial dilutions were added to an ELISA plate at RT for 1 h, and washed with PBST. Then the samples were stained with goat anti-human IgG Fc-HRP at RT for 1 h, and ABTS containing 30% H_2O_2 was added to detect the antigen binding ability through absorbance 405 nm. A linear interpolation method was used to calculate the EC_{50} of each group.

4.3 | Examination of the protease cleavage efficiency of the pro-Nivolumab IgG's LC and HC by western blot

To accurately examine any alterations in HC and LC molecular weight, we used pro-Nivolumab IgG, with a molecular weight of 51.63 kDa for the HC and 26.33 kDa for the LC. 1.11 μg of pro-Nivolumab IgG was incubated with 2 ng of activated MMP-2 (Sino Biological, 10082-HNAH, the specific activity is >1000 pmoles/min/

μg with fluorogenic peptide substrate Mca-PLGL-Dpa-AR-NH2 AnaSpec, Catalog # 27076) in 250:1 ratio at 37°C for 0, 1, 5, 10, 30, 60 or 90 min. All samples were boiled for 10 min under reducing conditions and separated by 10% SDS-PAGE and transferred to nitrocellulose membranes. After blocking with 5% skim milk diluted in phosphate-buffered saline at 4°C overnight, the membranes were stained with goat anti-human IgG Fc-HRP and goat anti-human IgG $F(ab')_2$-HRP secondary antibodies (Jackson ImmunoResearch Laboratories, West Grove, PA, USA) at RT for 1 h. The molecular weight of Pro-Nivolumab IgG-HC/LC was detected using a chemiluminescent detection system (UVP). We performed two independent experiments ($n = 2$). The chemiluminescent signal intensities were quantified by Gel-Pro Analyzer software.

4.4 | Examination of the molecular mass of pro-Nivolumab IgG by using MALDI-MS

The sinapinic acid (SA) matrix was used for protein analysis in MALDI-MS. The sample of Pro-Nivolumab was digested by MMP2 at 37°C for 0 and 90 min, and the cleavage was stopped by adding dithiothreitol to final concentration of 4 mM. The digested mixture was delivered into water by Amicon® Ultra Centrifugal Filter (10 kDa MWCO). Protein sample in water (1 μL) was spotted directly on the MALDI plate (MTP AnchorChip 600/384) and then immediately added with 1 μL matrix solution (33 mg/mL SA in 50% Acetonitrile containing 0.1% Trifluoroacetic acid). After the sample on MALDI plate was dried, their molecular weights were analyzed using an AutoFlex III MALDI-TOF (Bruker Daltonics, Bremen, Germany) in the m/z range of 4000–200,000.

4.5 | Determining the structural features by SWAXS experiments

The SEC-SAXS system included a micro-focused X-ray beam (400 × 200 μm^2), in-vacuum Eiger X 9M and X 1M detectors coupled with an in-line HPLC unit (Agilent 1260 series), and a Bio SEC-3 silica-based column (pore size 300 Å, Agilent). The column was equilibrated with a buffer containing 20 mM Tris–HCl pH 8.0, 150 mM/1 M NaCl, and 1 mM 2-mercaptoethanol. After the equilibration, 10.56 mg/mL of 99.05% purified pro-Nivolumab in 20 mM Tris 100 mM NaCl pH 8 was sent to the column, 100 μL of Cep57N at 5 mg/mL was loaded onto the column with a flow rate of 0.35 mL/min at 10°C. The eluate from the SEC run was directed to the SAXS system. The scattering data were collected with a frame rate of 2 s per frame (0.2 s between frames) over the elution peak. The sample stage and the detecting system comprising Eiger X 1M for WAXS and Eiger X 9M for SAXS data collections were located in the end-station zone. The spherical harmonics used is a set of expansion functions commonly used in structure model analysis in SAXS and WAXS region, as detailed in many reports (Franke et al., 2017). Data were background subtracted and analyzed using National Synchrotron Radiation Research Center TPS13A SAXS Data Reduction Kit (Ver. 3.6) (Shih et al., 2022) and ATSAS 3.2.1 (Manalastas-Cantos et al., 2021). The detailed SWAXS method table is in the Table S1.

4.6 | MD simulations to model the pro-Nivolumab Fab's mobile conformation

In MD simulations, we generated a model of pro-Nivolumab by applying the crystal structure of Nivolumab Fab (PDB ID: 5GGQ (Lee et al., 2016)). We attached the sequences of the Ab lock to the N-terminals of the LC and HC to model the Ab lock. Subsequently, the disulfide bonds in the Ab lock were formed by using DS modeling (BIOVIA Discovery Studio, 2018) for initial geometry clean and energy minimization by AMBER22 (Case, Duke, et al., 2022). The generated structure of pro-Nivolumab was checked by using the VMD software package (Humphrey et al., 1996) for protein checking and fixing the cis-peptide and chirality errors (Schreiner et al., 2011). The structure was then solvated in a 15 Å extending periodic box of TIP3P water using Leap from AmberTools22 (Case, Aktulga, et al., 2022). We conducted 64 sets of MD simulations with different initial velocities for 200 ps heating, 40 ns equilibrium, and 200 ns production steps at 300 K in NVT ensembles. The recorded trajectories were further categorized using K-means algorithm into 20 representative clusters based on the structures of the Ab lock region by using the cpptraj program (Roe & Cheatham, 2013).

4.7 | CRYSOL settings for generating theoretical SWAXS profiles from MD trajectories

To obtain theoretical SWAXS curves of the MD trajectories, we extracted PDB structure files using the cpptraj program. The PDB files were inputted to CRYSOL program (Manalastas-Cantos et al., 2021), using the command arguments of lm = 100 as the maximum order of spherical harmonics to enhance the resolution and fb = 18 to describe the surface of the macromolecule.

The constant argument was applied to prevent possible systematic errors due to mismatched buffers in the experimental data and the smax = 1.4 is used to involve the WAXS region (Svergun et al., 1995). After theoretical scattering profiles of all MD trajectories were derived, the average and standard derivation of all profiles were calculated at each q value.

4.8 | Using the genetic algorithm program for finding optimal volume fractions of EOM

To derive the optimal volume fraction of EOM that fits the SWAXS data, we selected 3200 snapshots from the MD trajectories as the structural pool. We developed a simple Python program that performs several functions: it runs CRYSOL to calculate theoretical SWAXS intensities for all PDB files in a specified folder, collects these intensities, and uses a genetic algorithm to find the optimal volume fractions. In our genetic algorithm setup, we began with 1000 individuals, each representing random combinations of volume fractions. Throughout the process, individuals underwent crossover at a rate of 20% and mutation at a rate of 80%. After generating 3000 candidates, we selected the top five performing and the bottom 10 performing candidates for the next generation, while the selection of other candidates was randomized based on their fit (proportional to $1/\chi^2$). This procedure was repeated across ca. 1–3 million generations. We ran the algorithm three times to ensure reliability, and the results consistently showed that the best EOM fits were nearly identical. The code for this program is available at https://sourceforge.net/projects/genetic-algorithm-for-eom/.

4.9 | The calculation of cover rates of each antigen-binding residue

The cover rate was calculated from the blocking frequencies of the CDR residues. A CDR residue was counted as covered if any atom of the Ab lock reaches above 120° and within 4 Å of any atom of the CDR residues. The cover rate of i-th residue was calculated by the following equation:

$$\text{Cover rate}_i = \left(\frac{C_i}{N}\right) \quad (1)$$

where the C_i is the counted blocked times of each CDR residue of all production trajectories. N is the number of snapshots of all trajectories. The heatmap was made by merging the cover rates as the occupancy parameter in PDB file and displayed by DS Modeling software (BIOVIA Discovery Studio, 2018).

4.10 | Deriving PASA of the substrates in the pro-Nivolumab LC and HC from structural information

We calculated the PASA of the MMP-2 substrates in the pro-Nivolumab LC and HC using the FreeSASA program (Mitternacht, 2016) with a 40 Å probe, based on the structural data from PDB:3AYU. A comparative analysis using a 70 Å probe from PDB:1GXD was also conducted; however, the 40 Å probe demonstrated a more suitable fit for our purposes. Within the GPLGVR sequence of MMP-2-substrate, LGV residues must be wrapped into the MMP-2- enzymatic site in cleavage, and thus the PASA values were calculated on these three residues. The minimum PASA value of the LGV residues was taken as an indicator of simultaneous contact. Each MD snapshot was outputted as a PDB file by cpptraj and inputted into FreeSASA program. The probe radius was set as 40 Å, and 40 slices per atom was set because the tested results were not obviously different from the more precise setting of 100 slices. After the PASA were derived for all MD trajectories, all PASA average of the LC and HC were averaged to gain the PASA value to estimate the protease cleavage efficiencies.

4.11 | Docking simulations on 20 representative cluster structures to validate the PASA methodology

HDOCK (Yan et al., 2020) was applied to docking simulations, which uses FFT-based global docking algorithm for rotational sampling at a rotational angle interval of 15° for FFT-based translational search. For each rotation, the top 10 translations with best shape complementarities are further optimized. Thus, a total of 4392 samples were derived in a docking run, and further clustered with a RMSD cutoff of 5 Å. At initial docking settings, the MMP-2 catalytic site (H119 and H123) is set as ligand docking site, and the LGV residues of the LC and HC are set as receptor docking site. The docking simulations were performed on 20 representative cluster structures on the purpose of time-saving and representing the original MD trajectories. The docking results were further filtered by the limitation that the distance between H119 of MMP-2 and the G residue of LGV must be within 6 Å to ensure the docking results fitting the orientation of the protease reaction. A docking pose was considered as

accessible if the G residue was positioned within 6 Å of MMP-2's H119, without the necessity of atomic-level docking alignment. This method provided an approximation of the accessibility under the rigid docking protocols. The number of filtered poses from LC and HC was summarized and further multiplied by the fraction of the MD ensembles for the final number of docking poses from LC and HC.

4.12 | Additional experiments of Nivolumab and Urelumab pro-Abs

The ELISA assays for antigen-binding ability of pro-Urelumab IgG-1 and -2 used the 4-1BB protein (R&D Systems, 838-4B-100) as the coated antigen. ELISA plate was blocked with DMEM/2% BSA at 37°C for 2 h. 100 nM Urelumab IgG and pro-Urelumab IgG-1 and -2 were incubated with or without 0.36 μg activated MMP-2 (Sino Biological, 10082-HNAH, the specific activity is >1000 pmoles/min/μg with fluorogenic peptide substrate Mca-PLGL-Dpa-AR-NH2 AnaSpec, Catalog # 27076) at 37°C for 1 h, and BCS was added to stop the reaction. The mole ratio of IgG to MMP-2 was increased to 50:1 because the cleavage rates of Urelumab were relative lower. All samples ($n = 2$) with serial dilutions were added to an ELISA plate at RT for 1 h and washed with PBST. Then the samples were stained with goat anti-human kappa chain-biotin at RT for 1 h and washed with PBST. Then the samples were stained with SA-HRP at RT for 1 h. After washing with PBST, ABTS containing 30% H_2O_2 was added to detect the antigen-binding ability through an absorbance of 405 nm. A linear interpolation method was used to calculate the EC_{50} of each group.

4.13 | Estimation of the cover rates of the binding residues for Nivolumab and Urelumab pro-Abs

The selection of binding residues was guided by the presence of significant hydrogen bonds or hydrophobic interactions with the antigen. For Nivolumab, the binding residues identified include H31N, H52W, H53Y, H99N, H100D, H101D, H102Y, L32Y, L49Y, and L50D, referencing PDB: 5WT9. In the case of Urelumab, the binding residues determined are H52N, H56Y, H103N, H104Y, H106W, L32Y, L93N, and L94W, referencing PDB: 6MHR. To calculate the cover rates for a pro-Ab, the cover rates of these binding residues are averaged, providing a measure of the effective binding site blocking by the Ab lock.

4.14 | Estimation of cleavage reaction rates for Nivolumab and Urelumab pro-Abs

The cleavage reaction rates of the Nivolumab and Urelumab pro-Abs were estimated by analyzing the time–concentration curves derived from Western blot data. These curves were fitted using the secondary reaction model as expressed in Equation (2).

$$\frac{d[S]}{dt} = -k_{\text{obs}}[E][S] \tag{2}$$

where the $[S]$ represents the concentration of the substrate, specifically the uncleaved pro-Ab's HC or LC. $[E]$ is the concentration of protease and k_{obs} is the observed cleavage rate, and t is the time in minutes. Integration of Equation (2) yields the following relationship (Equation 3):

$$\frac{[S]}{[S_0]} = \exp\exp\left(-k_{\text{obs}}[E]t\right) \tag{3}$$

where $[S_0]$ is the initial concentration of the pro-Ab chains. Considering the half-life of the reaction where the $[S]$ is $[S_0]/2$, Equation (4) is used to calculate the reaction rate:

$$k_{\text{obs}} = \frac{0.693}{[E]t_{1/2}} \tag{4}$$

because the peaks in Western blot were unstable and difficult for determining the concentration. We used the estimated half-lives of the Western blot to estimate the cleavage reaction rates of the MMP-2 proteases on the pro-Abs' LC and HC chains, as described in Equation (4).

AUTHOR CONTRIBUTIONS

Jun Min Liao: Methodology; software; writing – original draft; writing – review and editing; investigation; conceptualization; data curation; formal analysis; visualization; project administration. **Shih-Ting Hong:** Conceptualization; methodology; data curation; investigation; formal analysis; writing – original draft; writing – review and editing. **Yeng-Tseng Wang:** Methodology; software; investigation; supervision; resources. **Yi-An Cheng:** Methodology; data curation; investigation; validation; supervision. **Kai-Wen Ho:** Methodology; formal analysis; data curation. **Shu-Ing Toh:** Methodology; formal analysis; data curation. **Orion Shih:** Methodology; software; data curation; formal analysis; validation; visualization; project administration; writing – original draft; writing – review and editing. **U-Ser Jeng:** Methodology;

software; resources; data curation; validation; writing – review and editing. **Ping-Chiang Lyu:** Conceptualization; methodology; software; data curation; formal analysis; validation; investigation; writing – original draft. **I-Chen Hu:** Methodology; software; formal analysis; writing – original draft; writing – review and editing; validation. **Ming-Yii Huang:** Resources; formal analysis. **Chin-Yuan Chang:** Conceptualization; methodology; software; data curation; supervision; formal analysis; validation; investigation; funding acquisition; resources. **Tian-Lu Cheng:** Conceptualization; supervision; funding acquisition; resources; project administration; writing – original draft; writing – review and editing.

AFFILIATIONS

[1]Drug Development and Value Creation Research Center, Kaohsiung Medical University, Kaohsiung, Taiwan
[2]Graduate Institute of Medicine, College of Medicine, Kaohsiung Medical University, Kaohsiung, Taiwan
[3]Department of Biochemistry, Kaohsiung Medical University, Kaohsiung, Taiwan
[4]Department of Biomedical Science and Environmental Biology, Kaohsiung Medical University, Kaohsiung, Taiwan
[5]Precisemab Biotech Co. Ltd, Taipei, Taiwan
[6]Department of Biological Science and Technology, National Yang Ming Chiao Tung University, Hsinchu, Taiwan
[7]National Synchrotron Radiation Research Center, Hsinchu Science Park, Hsinchu, Taiwan
[8]Department of Chemical Engineering &College of Semiconductor Research, National Tsing Hua University, Hsinchu, Taiwan
[9]Institute of Bioinformatics and Structural Biology, National Tsing Hua University, Hsinchu, Taiwan
[10]Department of Radiation Oncology, Kaohsiung Medical University Hospital, Kaohsiung Medical University, Kaohsiung, Taiwan
[11]Center for Intelligent Drug Systems and Smart Biodevices, National Yang Ming Chiao Tung University, Hsinchu, Taiwan
[12]Department of Medical Research, Kaohsiung Medical University Hospital, Kaohsiung, Taiwan

ACKNOWLEDGMENTS

We thank U-Ser Jeng and Orion Shih at National Synchrotron Radiation Research Center for SWAXS analysis, and Ping-Chiang Lyu and I-Chen Hu at National Tsing Hua University for X-ray crystallography and MS. We appreciate Academia Sinica Cryo-EM Facility for testing the cyro-EM of pro-Nivolumab, and Miranda Loney for English editing.

FUNDING INFORMATION

This work was supported by grants from the Ministry of Science and Technology, Taipei, Taiwan (MOST 110-2320-B-037-010-MY3, MOST 111-2124-M-037-001-MY3, and MOST 111-2314-B-037-051-MY3); the KMU-KMUH Co-Project of Key Research (KMUH-DK(B) 110004-3, KMUH-DK(B)110006-1, KMUH-DK(B) 110006-2, KMUH-DK(B)111004-2, KMUH-DK(B) 111001-3, and KMUH-DK(B)112001-2); and the Research Foundation (KMU-DK(B)110004-2, KMU-DK(B)111004, KMU-DK(B)111001-2, KMU-DK(B)112001-1, and KMU-DK(B)112001-3) from Kaohsiung Medical University, Kaohsiung, Taiwan. This study was also supported partially by Kaohsiung Medical University Research Center Grant (Drug Development and Value Creation Research Center) (KMU-TC112A03) and NTHU-KMU Joint Research Project (KT112P002 and KT113P004).

CONFLICT OF INTEREST STATEMENT

All authors declare that they have no competing interests.

DATA AVAILABILITY STATEMENT

The SWAXS data of pro-Nivolumab are submitted to SASBDB (Kikhney et al., 2020) with the temporary accession https://www.sasbdb.org/data/SASDSN8/sjo5xyyls9. These data will be released at publication. The sequences of pro-Nivolumab and the additional pro-Abs are listed in Supplementary information.

ORCID

Tian-Lu Cheng https://orcid.org/0000-0002-7263-2766

REFERENCES

Biewenga L, Vermathen R, Rosier BJ, Merkx M. A generic antibody-blocking protein that enables pH-switchable activation of antibody activity. ACS Chem Biol. 2023;19:48–57.

BIOVIA, Dassault Systèmes, BIOVIA Discovery Studio. Discovery studio visualizer. San Diego: Dassault Systèmes; 2018.

Burley SK, Bhikadiya C, Bi C, Bittrich S, Chao H, Chen L, et al. RCSB protein data Bank: tools for visualizing and understanding biological macromolecules in 3D. Protein Sci. 2022;31:e4482.

Cao C, Xu N, Zheng X, Zhang W, Lai T, Deng Z, et al. Elevated expression of MMP-2 and TIMP-2 cooperatively correlates with risk of lung cancer. Oncotarget. 2017;8:80560.

Case D, Aktulga H, Belfon K, Ben-Shalom I, Brozell S, Cerutti D, et al. AmberTools22. San Francisco, CA: University of California; 2022.

Case DA, Duke RE, Walker RC, Skrynnikov NR, Cheatham TE III, Mikhailovskii O, et al. AMBER 22 reference manual. San Francisco, CA: University of California; 2022.

Cludts I, Spinelli FR, Morello F, Hockley J, Valesini G, Wadhwa M. Anti-therapeutic antibodies and their clinical impact in patients treated with the TNF antagonist adalimumab. Cytokine. 2017;96:16–23.

Desnoyers LR, Vasiljeva O, Richardson JH, Yang A, Menendez EE, Liang TW, et al. Tumor-specific activation of an EGFR-targeting probody enhances therapeutic index. Sci Transl Med. 2013;5:207ra144.

Ding Y, Zhang H, Zhong M, Zhou Z, Zhuang Z, Yin H, et al. Clinical significance of the uPA system in gastric cancer with peritoneal metastasis. Eur J Med Res. 2013;18:1–7.

Donaldson JM, Kari C, Fragoso RC, Rodeck U, Williams JC. Design and development of masked therapeutic antibodies to limit off-target effects: application to anti-EGFR antibodies. Cancer Biol Ther. 2009;8:2147–52.

Dong W, Li H, Zhang Y, Yang H, Guo M, Li L, et al. Matrix metalloproteinase 2 promotes cell growth and invasion in colorectal cancer. Acta Biochim Biophys Sin. 2011;43:840–8.

Drummer HE. Challenges to the development of vaccines to hepatitis C virus that elicit neutralizing antibodies. Front Microbiol. 2014;5:329.

Eatemadi A, Aiyelabegan HT, Negahdari B, Mazlomi MA, Daraee H, Daraee N, et al. Role of protease and protease inhibitors in cancer pathogenesis and treatment. Biomed Pharmacother. 2017;86:221–31.

Franke D, Petoukhov M, Konarev P, Panjkovich A, Tuukkanen A, Mertens H, et al. ATSAS 2.8: a comprehensive data analysis suite for small-angle scattering from macromolecular solutions. J Appl Cryst. 2017;50:1212–25.

Gupta R. SARS-CoV-2 omicron spike mediated immune escape and tropism shift. Res Sq. 2022;rs.3.rs-1191837.

Habič A, Novak M, Majc B, Lah Turnšek T, Breznik B. Proteases regulate cancer stem cell properties and remodel their microenvironment. J Histochem Cytochem. 2021;69:775–94.

Harris LJ, Larson SB, Hasel KW, McPherson A. Refined structure of an intact IgG2a monoclonal antibody. Biochemistry. 1997;36:1581–97.

Harris LJ, Skaletsky E, McPherson A. Crystallographic structure of an intact IgG1 monoclonal antibody. J Mol Biol. 1998;275:861–72.

Huang B-C, Lu Y-C, Liao J-M, Liu H-J, Hong S-T, Hsieh Y-C, et al. Development of a structure-based computational simulation to optimize the blocking efficacy of pro-antibodies. Chem Sci. 2021;12:9759–69.

Humphrey W, Dalke A, Schulten K. VMD: visual molecular dynamics. J Mol Graph. 1996;14:33–8.

Ilkovitch D, Lopez DM. Urokinase-mediated recruitment of myeloid-derived suppressor cells and their suppressive mechanisms are blocked by MUC1/sec. Blood. 2009;113:4729–39.

Joshi H, Cheluvaraja S, Somogyi E, Brown DR, Ortoleva P. A molecular dynamics study of loop fluctuation in human papillomavirus type 16 virus-like particles: a possible indicator of immunogenicity. Vaccine. 2011;29:9423–30.

Kikhney AG, Borges CR, Molodenskiy DS, Jeffries CM, Svergun DI. SASBDB: towards an automatically curated and validated repository for biological scattering data. Protein Sci. 2020;29:66–75.

Klein A, Rovó P, Sakhrani VV, Wang Y, Holmes JB, Liu V, et al. Atomic-resolution chemical characterization of (2x) 72-kDa tryptophan synthase via four-and five-dimensional 1H-detected solid-state NMR. Proc Natl Acad Sci. 2022;119:e2114690119.

Lavie M, Hanoulle X, Dubuisson J. Glycan shielding and modulation of hepatitis C virus neutralizing antibodies. Front Immunol. 2018;9:910.

Lee JY, Lee HT, Shin W, Chae J, Choi J, Kim SH, et al. Structural basis of checkpoint blockade by monoclonal antibodies in cancer immunotherapy. Nat Commun. 2016;7:13354.

Li H, Qiu Z, Li F, Wang C. The relationship between MMP-2 and MMP-9 expression levels with breast cancer incidence and prognosis. Oncol Lett. 2017;14:5865–70.

Li Y, Cozzi P. Targeting uPA/uPAR in prostate cancer. Cancer Treat Rev. 2007;33:521–7.

Li Y, Zhang C, Li G, Deng G, Zhang H, Sun Y, et al. Protease-triggered bioresponsive drug delivery for the targeted theranostics of malignancy. Acta Pharm Sin B. 2021;11:2220–42.

Likas A, Vlassis N, Verbeek JJ. The global k-means clustering algorithm. Pattern Recognit. 2003;36:451–61.

Lin SW, Su KH, Yeh YQ, Jeng US, Wu CM, Yang HC. Molecular dynamics simulation combined with small-angle X-ray/neutron scattering defining solution-state protein structures. J Chin Chem Soc. 2021;68:403–8.

Liu D-G, Chang C-H, Chiang L-C, Lee M-H, Chang C-F, Lin C-Y, et al. Optical design and performance of the biological small-angle X-ray scattering beamline at the Taiwan photon source. J Synchrotron Radiat. 2021;28:1954–65.

Lu Y-C, Chuang C-H, Chuang K-H, Chen I-J, Huang B-C, Lee W-H, et al. Specific activation of pro-infliximab enhances selectivity and safety of rheumatoid arthritis therapy. PLoS Biol. 2019;17:e3000286.

Lucchi R, Bentanachs J, Oller-Salvia B. The masking game: design of activatable antibodies and mimetics for selective therapeutics and cell control. ACS Cent Sci. 2021;7:724–38.

Manalastas-Cantos K, Konarev PV, Hajizadeh NR, Kikhney AG, Petoukhov MV, Molodenskiy DS, et al. ATSAS 3.0: expanded functionality and new tools for small-angle scattering data analysis. J Appl Cryst. 2021;54:343–55.

Martínez L. Automatic identification of mobile and rigid substructures in molecular dynamics simulations and fractional structural fluctuation analysis. PLoS One. 2015;10:e0119264.

Mendes M, Mahita J, Blazeska N, Greenbaum J, Ha B, Wheeler K, et al. IEDB-3D 2.0: structural data analysis within the immune epitope database. Protein Sci. 2023;32:e4605.

Meng B, Ferreira IA, Abdullahi A, Goonawardane N, Saito A, Kimura I, et al. SARS-CoV-2 omicron spike mediated immune escape and tropism shift. BioRxiv. 2021. https://doi.org/10.1101/2021.12.17.473248

Mitternacht S. FreeSASA: an open source C library for solvent accessible surface area calculations. F1000Res. 2016;5:189.

Nixon J, Newbold P, Mustelin T, Anderson GP, Kolbeck R. Monoclonal antibody therapy for the treatment of asthma and chronic obstructive pulmonary disease with eosinophilic inflammation. Pharmacol Ther. 2017;169:57–77.

Pavón MA, Arroyo-Solera I, Céspedes MV, Casanova I, León X, Mangues R. uPA/uPAR and SERPINE1 in head and neck cancer: role in tumor resistance, metastasis, prognosis and therapy. Oncotarget. 2016;7:57351–66.

Piai A, Hošek T, Gonnelli L, Zawadzka-Kazimierczuk A, Koźmiński W, Brutscher B, et al. "CON-CON" assignment strategy for highly flexible intrinsically disordered proteins. J Biomol NMR. 2014;60:209–18.

Punjani A, Fleet DJ. 3D flexible refinement: structure and motion of flexible proteins from cryo-EM. BioRxiv. 2021. https://doi.org/10.1101/2021.04.22.440893

Ras-Carmona A, Pelaez-Prestel HF, Lafuente EM, Reche PA. BCEPS: a web server to predict linear B cell epitopes with enhanced immunogenicity and cross-reactivity. Cells. 2021;10:2744.

Roe DR, Cheatham TE III. PTRAJ and CPPTRAJ: software for processing and analysis of molecular dynamics trajectory data. J Chem Theory Comput. 2013;9:3084–95.

Röllen K, Granzin J, Batra-Safferling R, Stadler AM. Small-angle X-ray scattering study of the kinetics of light-dark transition in a LOV protein. PLoS One. 2018;13:e0200746.

Scapin G, Yang X, Prosise WW, McCoy M, Reichert P, Johnston JM, et al. Structure of full-length human anti-PD1 therapeutic IgG4 antibody pembrolizumab. Nat Struct Mol Biol. 2015;22:953–8.

Schneidman-Duhovny D, Pellarin R, Sali A. Uncertainty in integrative structural modeling. Curr Opin Struct Biol. 2014;28:96–104.

Schreiner E, Trabuco LG, Freddolino PL, Schulten K. Stereochemical errors and their implications for molecular dynamics simulations. BMC Bioinformatics. 2011;12:190.

Schumann W, Loschwitz J, Reiners J, Degrandi D, Legewie L, Stühler K, et al. Integrative modeling of guanylate binding protein dimers. Protein Sci. 2022;32:e4818.

Self CH, Thompson S. Light activatable antibodies: models for remotely activatable proteins. Nat Med. 1996;2:817–20.

Shih O, Liao K-F, Yeh Y-Q, Su C-J, Wang C-A, Chang J-W, et al. Performance of the new biological small-and wide-angle X-ray scattering beamline 13A at the Taiwan photon source. J Appl Cryst. 2022;55:340–52.

Song L, Lu L, Huang W, Ravikumar KM, Meng J, Yang S. Integrative SAXS-driven computational modeling of biomolecular complexes. In: Fan C, Zhao Z, editors. Synchrotron radiation in materials science: light sources, techniques, and applications. Volume 2. Hoboken, NJ: Wiley; 2018. p. 657–85.

Svergun D, Barberato C, Koch MH. CRYSOL–a program to evaluate X-ray solution scattering of biological macromolecules from atomic coordinates. J Appl Cryst. 1995;28:768–73.

Takeuchi T, Hayashi M, Tamita T, Nomura Y, Kojima N, Mitani A, et al. Discovery of aryloxyphenyl–heptapeptide hybrids as potent and selective matrix metalloproteinase-2 inhibitors for the treatment of idiopathic pulmonary fibrosis. J Med Chem. 2022;65:8493–510.

Tang Z, Wang X, Tang M, Wu J, Zhang J, Liu X, et al. Overcoming the on-target toxicity in antibody-mediated therapies via an indirect active targeting strategy. Adv Sci. 2023;10:2206912.

Tian D, Sun Y, Zhou J, Ye Q. The global epidemic of SARS-CoV-2 variants and their mutational immune escape. J Med Virol. 2022;94:847–57.

Trang VH, Zhang X, Yumul RC, Zeng W, Stone IJ, Wo SW, et al. A coiled-coil masking domain for selective activation of therapeutic antibodies. Nat Biotechnol. 2019;37:761–5.

Uversky VN. Unusual biophysics of intrinsically disordered proteins. Biochim Biophy Acta. 2013;1834:932–51.

Van Den Bedem H, Fraser JS. Integrative, dynamic structural biology at atomic resolution—it's about time. Nat Methods. 2015;12:307–18.

Villarreal SA, Stewart PL. CryoEM and image sorting for flexible protein/DNA complexes. J Struct Biol. 2014;187:76–83.

Wright PE, Dyson HJ. Intrinsically disordered proteins in cellular signalling and regulation. Nat Rev Mol Cell Biol. 2015;16:18–29.

Yan Y, Tao H, He J, Huang S-Y. The HDOCK server for integrated protein–protein docking. Nat Protoc. 2020;15:1829–52.

Yang S, Park S, Makowski L, Roux B. A rapid coarse residue-based computational method for X-ray solution scattering characterization of protein folds and multiple conformational states of large protein complexes. Biophys J. 2009;96:4449–63.

Zhou H, Guterres H, Mattos C, Makowski L. Predicting X-ray solution scattering from flexible macromolecules. Protein Sci. 2018;27:2023–36.

SUPPORTING INFORMATION

Additional supporting information can be found online in the Supporting Information section at the end of this article.

How to cite this article: Liao JM, Hong S-T, Wang Y-T, Cheng Y-A, Ho K-W, Toh S-I, et al. Integrating molecular dynamics simulation with small- and wide-angle X-ray scattering to unravel the flexibility, antigen-blocking, and protease-restoring functions in a hindrance-based pro-antibody. Protein Science. 2024;33(9):e5124. https://doi.org/10.1002/pro.5124